

Photo-homogenization assisted segregation easing technique (PHASET) for highly efficient and stable wide-bandgap perovskite solar cells

Received: 13 March 2025

Accepted: 12 August 2025

Published online: 29 August 2025



Liming Du^{1,2,6}, Fangfang Cao^{3,6}, Rui Meng^{1,2,6}, Yueying Zhang³, Junchuan Zhang³, Zhiyu Gao⁴, Cong Chen⁴, Can Li^{1,2}, Dewei Zhao⁴, Jichun Ye³, Zhen Li^{1,2}✉ & Chuanxiao Xiao^{3,5}✉

Wide-bandgap (WBG) perovskite solar cells (PSCs) can exceed the Shockley–Queisser limit in tandem solar cells (TSCs), but phase segregation under continuous illumination limits their stability. Using in-situ microscopic characterizations, we investigate the dynamics of photon-induced phase segregation. Initial light soaking drives iodide diffusion into a metastable state, but continued redistribution increases the phase separation energy barrier, resulting in a more stable, segregation-resistant state. Inspired by stabilization methods in silicon photovoltaics, we develop the Photo-Homogenization Assisted Segregation Easing Technique (PHASET), which combines light soaking with 2-ThEABr surface passivation to suppress halide segregation. PHASET enhances efficiency and stability, enabling an efficiency of 20.23% for 1.79 eV WBG-PSCs, with 97% of the initial efficiency retained after 1200 hours of continuous illumination. Integration with a 1.25 eV narrow-bandgap subcell results in a two-terminal all-perovskite TSC with 28.64% efficiency, retaining 77% of its initial performance after 1200 hours of maximum power point tracking.

The versatility of organic-inorganic hybrid perovskite materials, characterized by their adjustable bandgap and straightforward preparation process, has positioned them as an appealing option for tandem solar cells (TSCs). These materials exhibit favorable optoelectronic properties, making them a strategic choice for enhancing power conversion efficiency (PCE) across various photovoltaic technologies^{1,2}. Currently, the certified efficiency of all-perovskite TSCs has soared to 30.1%³, surpassing the theoretical Shockley–Queisser (S–Q) radiative efficiency limit of single-junction solar cells. Moreover, wide-bandgap (WBG)

perovskite-based TSCs paired with lower bandgap materials, such as copper indium gallium selenide and perovskite, have displayed promising achievements, highlighting the potential of this approach in advancing solar cell technology^{3,4}.

Despite these advancements, TSCs face critical stability challenges, particularly with WBG perovskites (1.7–2.3 eV), commonly used as top cell absorbers^{5,6}. Achieving the target bandgap often involves adjusting the bromine-to-iodine ratio in the perovskite composition^{7–9}, as initially reported by Noh et al. in 2013, who showed that bromine

¹State Key Laboratory of Solidification Processing, Northwestern Polytechnical University, Xi'an, China. ²School of Materials Science and Engineering, Northwestern Polytechnical University, Xi'an, China. ³Ningbo Institute of Materials Technology and Engineering, Chinese Academy of Sciences, Ningbo, China. ⁴College of Materials Science and Engineering & Engineering Research Center of Alternative Energy Materials & Devices, Ministry of Education, Sichuan University, Chengdu, China. ⁵Ningbo New Materials Testing and Evaluation Center CO. Ltd, Ningbo, China. ⁶These authors contributed equally: Liming Du, Fangfang Cao, Rui Meng. ✉e-mail: lizhen@nwpu.edu.cn; cxiao@nimte.ac.cn

incorporation in $\text{MAPb}(\text{I}_{1-x}\text{Br}_x)_3$ creates a tunable bandgap from 1.57 to 2.3 eV¹. Unfortunately, introducing bromine in this manner can lead to halide segregation under continuous illumination, a phenomenon termed light-induced halide phase segregation^{10–16}. Hoke et al. observed in 2015 that phase segregation creates regions of bromine and iodine enrichment, leading to local fluctuations in bandgap and Fermi levels⁶. These changes generate crystal and interface defects, triggering nonradiative recombination and voltage losses, ultimately impacting both performance and long-term stability in WBG perovskite solar cells (PSCs)^{17–22}.

Efforts to mitigate phase segregation typically focus on halide migration control, achieved by introducing smaller cations or larger anions to increase the lattice distortion and energy barrier for iodine migration^{22–27}. Additionally, grain boundaries (GBs) and interfacial defects can be passivated to hinder ion migration pathways^{28–31}. However, a deeper microscopic understanding of the phase segregation process is essential to comprehensively address these stability issues and to develop robust and generalized strategies for long-term performance.

In this study, we use in-situ Kelvin probe force microscopy (KPFM) to explore the dynamic process of phase segregation in WBG perovskite materials with nanometer-scale resolution. By subjecting the films to cycles of light illumination and dark storage, we track the evolution of phase segregation and its subsequent recovery. During light soaking, iodine-rich regions with lower surface potential gradually mix into surrounding grains, leading to a more uniform halide distribution. Following dark storage, the surface potential returns to near-pristine levels, accompanied by enhanced contrast at GBs. Once homogenized by light-induced processes, the surface topography and potential remain stable under further illumination. Building on these insights, we develop a fabrication technique called **Photo-Homogenization Assisted Segregation Easing Technique (PHASET)**, combining light soaking with 2-ThEABr surface passivation. This approach involves post-annealing light soaking of Br-I mixed perovskite films, promoting halide ion redistribution to achieve a quasi-stable state and suppressing segregation. The 2-dimensional surface treatment further stabilizes mobile ions. Using PHASET, we achieve a significant improvement in the efficiency of 1.79 eV WBG PSCs, increasing from 16.71% to 20.23%. Additionally, device stability is greatly enhanced, with unencapsulated WBG-PSCs maintaining 97% of their initial PCE after 1200 h of continuous light soaking in nitrogen. These advancements enable the fabrication of all-perovskite TSCs with a champion efficiency of 28.64% with good operational stability, maintaining 77% of their initial PCE after 1200 h of continuous operation under 1-sun illumination. These findings provide a detailed understanding of phase segregation mechanisms and highlight PHASET as a promising strategy for fabricating high-performance, stable perovskite materials.

Results and discussion

We performed in-situ high spatial resolution KPFM and investigated changes of both topography and surface potential of 1.79 eV perovskite films with a composition of $\text{FA}_{0.8}\text{Cs}_{0.2}\text{Pb}(\text{I}_{0.6}\text{Br}_{0.4})_3$ (Supplementary Fig. 1). Initially, the pristine film exhibited mostly flat GBs and grain interiors (GIs), with minor topography and surface potential variations (Fig. 1a). However, surface potential mapping revealed small chunks (100–200 nm) with a lower potential (–150 mV) compared to surrounding areas, indicating a higher work function. These chunks are likely associated with the excess PbI_2 (5–10%) present in the non-stoichiometric precursor solution. Based on previous studies, the high work function chunks are attributed to PbI_2 -rich regions^{32,33}. As shown in state I, the iodine distribution was not homogeneous in the pristine film, with distinct iodine-enriched regions and iodine vacancies. This should arise from the excessive PbI_2 from the precursor solution. Scanning electron microscopy (SEM) and energy dispersive X-ray

spectroscopy (EDS) analysis confirmed that these regions were PbI_2 -rich with slightly higher levels of both iodine and lead than the surrounding film (Supplementary Fig. 2).

To improve the visualization, we added a rectangle around one grain to emphasize the observed changes. Over 5 h of illumination (see Supplementary Note 1 for lamp details), we observed a gradual decrease in potential contrast between the PbI_2 chunk and the surrounding film, while the topography remained relatively unchanged (Fig. 1b). This diminishing contrast suggests iodine diffusion into the surrounding areas. As shown in state II, continuous illumination promotes the formation of oxidized iodine species, increasing iodine's chemical activity^{34,35}. Iodide migration filled some vacancies, reducing the density of iodine vacancies and interstitial iodine³⁶. Rapid migration of ions along GBs led to an instantaneous equivalence of ion concentrations in the GIs, rendering the GBs indistinguishable. After illumination, the ions tend to diffuse back to their original sites (state III). Moreover, the chunk becomes more prominent in the topography (Fig. 1c, top), and two smaller potential spikes emerge in the potential map (Fig. 1c, middle). Notably, these spikes are not attributed to noise, as they persist across multiple scans. A more complete set of in-situ KPFM results is presented in Supplementary Figs. 3 and 4. It is noteworthy that the PbI_2 chunk and potential spikes eventually disintegrated into smaller particles (~50 nm), and no distinctive phenomena were observed at the GBs. The appearance of the prominent chunk and associated potential fluctuations may lead to nonradiative recombination in actual solar cell devices. Continuous light exposure drives ongoing segregation of iodine-rich areas, particularly in cases of initial unstable or nonuniform iodine distribution.

Following phase segregation, we stored the sample in the dark while continually monitoring the evolution of topography and surface potential. The surface potential continued to evolve slowly (Supplementary Figs. 5 and 6), indicating ongoing ion migration even in the absence of light. This behavior can be attributed to the concentration gradient driving iodide back toward its original position. After ~20 days of storage in the dark, the potential spikes disappeared, and the overall potential distribution returned to a stage similar to the initial, except that the contrast between GIs and GBs became more pronounced (Fig. 1d). Additionally, the topography analysis revealed the fragmentation of the PbI_2 chunk into smaller and separated particles. The iodide ions eventually settled into a new iodide distribution in equilibrium, which leads to the reappearance of the dark area in the surface potential (state IV). The higher potential at GBs suggests a localized positive charge state³⁷, likely due to fewer iodide ions. This built-in potential at GBs creates an energetic barrier that attracts electrons and repels holes from the GBs, which could enhance charge extraction and reduce carrier recombination³⁸. The reversion to the pristine stage implies that phase segregation is predominantly reversible, with the initial topography and surface potential distribution being favored and existing in a metastable state. Interestingly, after extended storage, we conducted another light and dark cycle, finding that both the topography and surface potential remained almost unchanged (Supplementary Figs. 7 and 8). After this cycle, the iodine ions and vacancies were reduced, with minimal iodide migration and trap complexation. These findings suggest that halide elements have reached a more stable thermodynamic state after completing the light and dark cycle.

We also used conductive atomic force microscopy (C-AFM) to study the microscopic conductivity properties before and after light soaking (Supplementary Fig. 9). Prior to the light soaking, certain areas exhibited lower conductivity, primarily concentrated near GBs. This less conductive area has a distribution pattern similar to the lower potential chunks shown in Fig. 1a, suggesting the areas may contain PbI_2 that has lower conductivity. After illumination, the conductivity distribution became more uniform. Additionally, the material corresponding to the region with lower conductivity appears to diffuse throughout the sample, leading to a reduction in the size of the lower

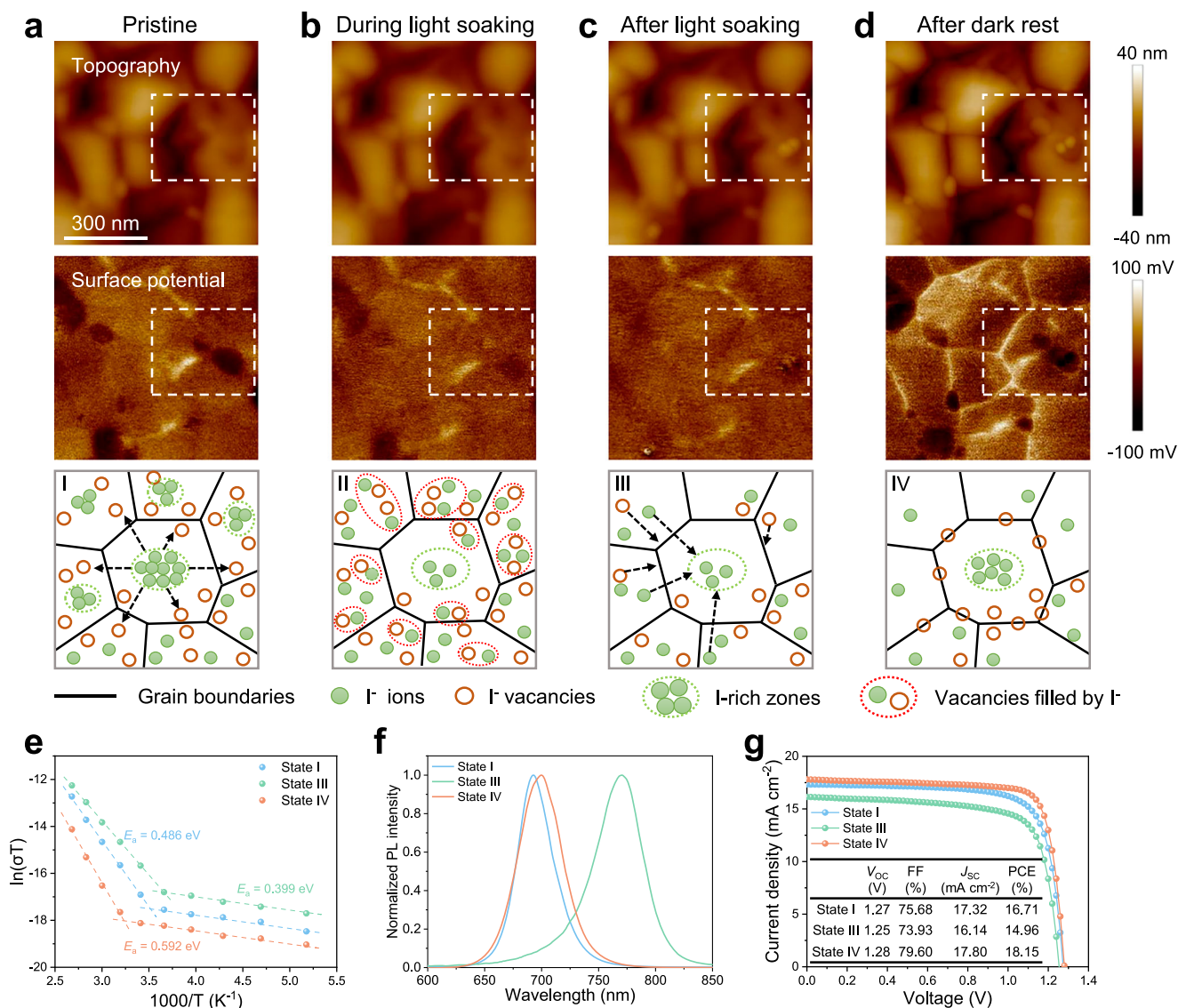


Fig. 1 | Dynamic process of light-induced halide phase segregation and recovery in WBG perovskite film. a–d In-situ KPFM mapping at the same position showing topography (top), surface potential (middle), and schematic (bottom) of the perovskite film. **a** Pristine state, **b** During light soaking, **c** After light soaking, and **d** After dark rest. Images were flattened to 0th order for improved contrast. The

white rectangle highlights noticeable topography and surface potential changes within one grain. **e** Ion migration activation energy derived from temperature-dependent conductivity measurements. **f** PL spectra of perovskite films with different states. **g** J – V curves of WBG PSCs at states I, III, and IV under reverse scan.

conductivity areas and a decrease in the overall current density. After dark storage for 240 h, the surface current distribution became even more uniform, with a lower overall current of 40 pA. This observed process aligns well with the KPFM results, reinforcing the link between ionic redistribution and the electrical properties of the film.

As previously discussed, halide inhomogeneity is a critical factor influencing the ion migration in a perovskite film. To investigate the ion migration in perovskite film at different states, we have evaluated the ion migration activation energy (E_a) of WBG perovskite films at States I, III, and IV using the Nernst-Einstein relationship, based on temperature-dependent electrical conductivity measurements^{39,40}. As shown in Fig. 1e, the E_a value is derived from the slope of the $\ln(\sigma T)$ versus $1000/T$ plot, where σ is the electrical conductivity, and T is the absolute temperature. The E_a is 0.486, 0.399, and 0.592 eV for WBG perovskite at States I, III, and IV, respectively. The higher E_a at State IV indicates suppressed ion migration as halide elements have reached a more stable thermodynamic state. This observed process aligns well with the in-situ KPFM and photoluminescence (PL) results, further

supporting the conclusion that ion redistribution stabilizes after completing the light and dark cycle.

To further explore the role of iodine ion migration in phase segregation, we introduced excess PbI_2 in fabricating perovskite films and examined them using in-situ PL spectroscopy. We used a 532 nm laser for over 600 s on the perovskite films with 0%, 5%, and 10% mol excess of PbI_2 , respectively. The PL intensities were normalized to facilitate the comparison of peak shifts. Initially, all three films showed an emission peak around 695 nm (State I), as illustrated in Fig. 1f and Supplementary Fig. 10a. After about 100 s of laser illumination (160 s for the film with 5% PbI_2 excess), a new emission peak emerged at ~770 nm, increasing in intensity while the original 695 nm peak persisted. These results confirmed the presence of phase segregation, consistent with a previous report⁴¹.

Following a 24 h light soaking (State III), the emission peaks of all three films completely red shifted to ~770 nm (Supplementary Fig. 11). After dark storage for 240 h (State IV), the peaks shifted back to ~705 nm (0% PbI_2), ~699 nm (5% PbI_2), and ~703 nm (10% PbI_2),

although they remained at longer wavelengths than their initial positions (Supplementary Fig. 11). This suggests that the phase separation process is partially reversible, especially in films with 5% mol excess of PbI_2 , and that iodine anions re-incorporate into the film after a light-dark cycle. Notably, the recovery of the phase segregation phenomenon takes longer than the process that occurs. We then performed another round of in-situ PL measurements for 600 s on these films that had undergone light-dark cycling (Supplementary Fig. 10b). The PL peaks showed minimal redshift, especially in films with 5% excess PbI_2 , and were only accompanied by a slight increase in the full-width at half maximum (FWHM). Additionally, we analyzed the average bandgap and its increase rate over time from the in-situ PL spectra to assess phase stability under laser illumination (Supplementary Fig. 12 and Supplementary Note 2). After light soaking for 24 h and dark storage, the rate of bandgap reduction slowed significantly, especially in the 5% PbI_2 film, where the bandgap decreased only from 1.77 eV to 1.75 eV, and the rate of bandgap increase approached zero. These findings indicate that the photostability of perovskite films with 5% excess PbI_2 improves after light illumination and dark recovery cycle.

In the subsequent part of this study, we used perovskite films with 5% mol excess PbI_2 . Supplementary Fig. 13 shows the optimization of light soaking time for perovskite thin films. During the first 1–2 h of light soaking and dark recovery overnight, the PL peak position remained stable, indicating minimal changes in the optical properties. However, with prolonged light exposure, the PL peak gradually redshifted, suggesting more pronounced phase segregation. We then fabricated devices with an ITO/ NiO_x /Me-4PACz/perovskite/ C_{60} /BCP/Ag structure, using perovskite films subjected to different light soaking durations and subsequent dark recovery (Supplementary Fig. 14). The current density-voltage (J - V) curves of champion PSCs light soaked from 0 to 8 h and dark recovery overnight are shown in Fig. 1g, Supplementary Figs. 15 and 16 and Supplementary Table 1. The statistical distributions of PCEs and other key photovoltaic parameters are presented in Supplementary Fig. 17, revealing that performance improvements were primarily driven by increases in open-circuit voltage (V_{OC}) and fill factor (FF). We further analyzed the relationship between PL peak position and average PCE of WBG PSCs as a function of light soaking time (Supplementary Fig. 18). Devices subjected to 2 h of light soaking achieved a peak efficiency of 17.90%, compared to 16.24% for pristine devices. This demonstrates that appropriate light treatment can enhance device performance. However, prolonged light soaking led to severe phase separation, beyond the film's ability to recover, causing a significant redshift in the PL peak and a gradual decline in performance.

KPFM, PL combined with J - V measurements revealed that light-induced halide redistribution effectively mitigates phase segregation in perovskite films, analogous to the light-induced degradation (LID) and subsequent regeneration observed in silicon solar cells. In LID of silicon solar cells, initial light exposure induces boron-oxygen defects, yet subsequent illumination or light treatment can expedite the transition through the degradation phase to a regenerated state where the defects are passivated and stabilization is achieved. Although not a fundamental solution, this approach has proven effective and is widely implemented in industrial silicon solar cell manufacturing^{42–46}. Additionally, prolonged illumination has been shown to mitigate light- and elevated-temperature-induced degradation (LeTID) by reverting hydrogen to a passivating charge state^{47,48}. These insights inspired us to develop a similar method in fabricating perovskite thin films, termed PHASET, to leverage the light-induced phase segregation and subsequent recovery to achieve phase-stable thin films with enhanced device performance.

While light soaking reduced defects and improved the bulk material quality, surface dangling bonds and vacancies persisted, facilitating ion migration. To mitigate this, we incorporated a previously published 2-ThEABr surface passivation step^{49,50} into the PHASET process. We further evaluated the phase stability of the films

using 600-s in-situ PL measurements. Compared to the pristine film, the 2h-light-soaked film exhibited a significantly reduced redshift in the PL peak position, and the secondary peak never surpassed the primary peak in intensity, while the PHASET film exhibited negligible changes, indicating suppressed phase segregation (Fig. 2a). The PHASET film exhibited a main PL emission peak maintaining a bandgap of 1.79 eV over 600 s (Fig. 2b and Supplementary Fig. 19). In contrast, untreated films showed a bandgap decrease to 1.67 eV, while light-soaked films showed a slower decline to 1.71 eV. Films treated with 2-ThEABr alone also exhibited phase segregation, with the main PL emission peak shifting to 1.77 eV (Supplementary Fig. 20). Meanwhile, we performed long-time (10 days) light-soaking aging tests on our WBG perovskite films in a nitrogen glove box to assess their stability. We used an LED (1-sun) light source, with an enclosed testing chamber at a temperature of -45°C due to the illumination. As depicted in Supplementary Fig. 21, the PL emission spectra of the four films peaked around 695 nm. After 1 day of aging, the pristine films showed broadening with a peak at 700 nm. Over subsequent days of light soaking, the film experienced further red shifting, and a new emission peak emerged at ~ 760 nm, increasing in intensity while the original 695 nm peak persisted. The significant peak redshift in the pristine film is mainly ascribed to the formation of I-rich domains. In contrast, the PL peak of PHASET film showed minimal change, with only a slight shift from 695 to 697 nm.

Figure 2c shows the phase segregation process and the PHASET schematic. During light soaking, halide ions diffuse and redistribute throughout the film. The perovskite film was reversibly cycled in the pristine (state A) and slightly phase segregation states (state B)⁵¹. Prolonged light soaking leads to a degraded state (State C), but appropriate treatment facilitates halide redistribution, quickly bypasses the degraded state, and enables regeneration to a stable phase (State D).

The KPFM measurements were then conducted to observe the effect of PHASET treatment on the topography and electrostatic potential distribution (Fig. 3a and Supplementary Figs. 22 and 23). The pristine film exhibits a relatively uniform potential with an average potential value of -450 mV. And we observed a large number of PbI_2 chunks with lower potential at -600 mV. The light-soaking-treated film has less pronounced regions with lower potential, indicating that light exposure facilitated the diffusion of iodine ions from the PbI_2 chunks into the surrounding areas. While for the 2-ThEABr-treated and PHASET films, the overall potential increased to -370 mV. More importantly, the GBs exhibit higher potentials than the GIs. These findings were consistent with the observation in Fig. 1.

X-ray diffraction (XRD) patterns (Fig. 3b) confirmed the improved crystallinity of light soaking-treated and PHASET-treated films. Although all films exhibited similar diffraction peaks, the PHASET samples showed narrower and more intense peaks, particularly for the (100) plane at -14.4° and the (110) plane. The (100) peak of the PHASET film exhibits an FWHM of 0.12° , which is narrower than that of 0.15° and 0.22° for the light soaking-treated and pristine films, respectively (Supplementary Fig. 24). This trend indicates improved crystallinity^{52,53}. A more intense PbI_2 peak is observed in the pristine film due to the 5 mol% excess of PbI_2 , but the PbI_2 peak intensity was reduced in the light soaking-treated and PHASET films, suggesting halide redistribution. The steady-state PL peak intensity of PHASET-treated quartz/perovskite films increased to 19592, compared to 9792 and 2156 for the light soaking-treated and pristine films, respectively (Fig. 3c). And time-resolved PL (TRPL) measurements (Fig. 3d) showed significantly improved carrier lifetimes. The average lifetime (τ_{avg}), calculated from bi-exponential fitting (Supplementary Table 2)^{54,55}, increased to 98.6 and 288.8 ns for the light soaking-treated and PHASET films, respectively, compared to 79.0 ns for the pristine film. These enhancements reflect reduced nonradiative recombination losses due to halide homogenization and defect reduction.

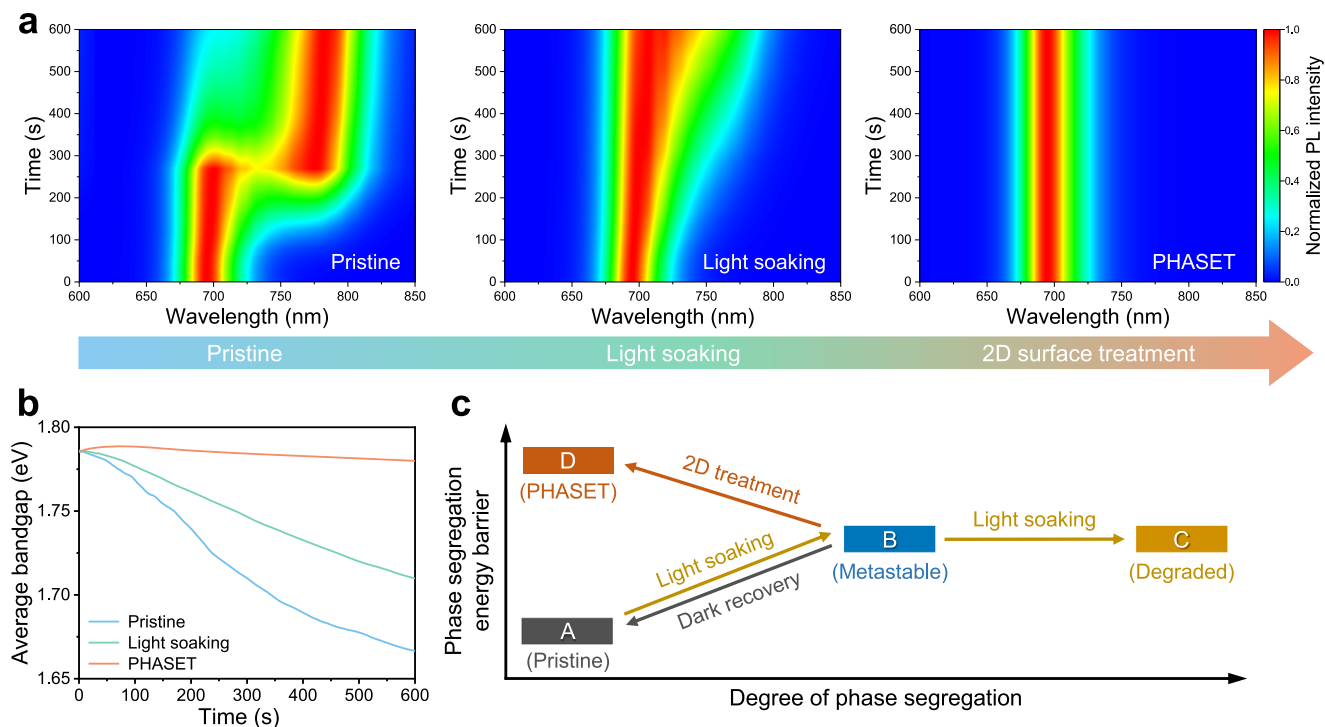


Fig. 2 | Properties of pristine, light soaking-treated, and PHASET perovskite films. **a** In-situ PL spectra evolution of pristine, light soaking-treated, and PHASET perovskite films under continuous illumination. **b** Evolution of average

bandgap values calculated from PL emission over time. **c** Schematic illustration of the proposed mechanism underlying the PHASET strategy.

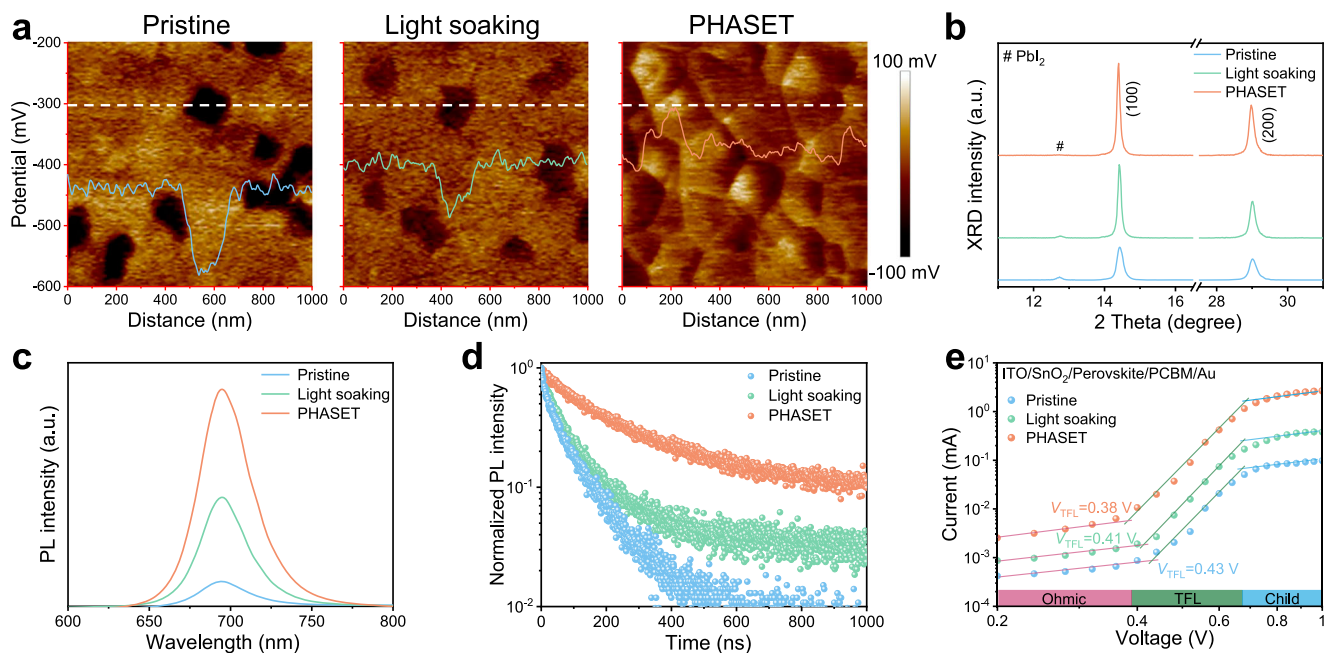


Fig. 3 | Characterization of pristine, light soaking-treated, and PHASET perovskite films. **a** KPFM surface potential maps and corresponding line profiles. Images were flattened to 0th order for improved contrast. **b** XRD patterns. **c** Steady-

state PL and **d** TRPL spectra. **e** SCLC measurements of electron-only devices fabricated using these perovskite films.

Trap density was assessed using space-charge-limited-current (SCLC) method with electron-only and hole-only devices. Figure 3e shows dark J - V curves for the electron-only device (ITO/SnO₂/perovskite/PCBM/Au). The trap-filled limit voltage (V_{TFL}) decreased from 0.43 V to 0.38 V, and the calculated electron trap density is $1.54 \times 10^{15} \text{ cm}^{-3}$ for the PHASET device, which is lower than the $1.74 \times 10^{15} \text{ cm}^{-3}$ of the pristine

device and $1.66 \times 10^{15} \text{ cm}^{-3}$ of the light soaking-treated device. A similar trend was observed in hole-only device structure (ITO/PEDOT:PSS/perovskite/PTAA/Au) in Supplementary Fig. 25. The V_{TFL} of pristine, light soaking-treated, and PHASET devices were 0.78 V, 0.67 V, and 0.60 V, with corresponding hole trap densities is $3.16 \times 10^{15} \text{ cm}^{-3}$, $2.71 \times 10^{15} \text{ cm}^{-3}$, and $2.43 \times 10^{15} \text{ cm}^{-3}$, respectively. The reduced trap densities confirm that

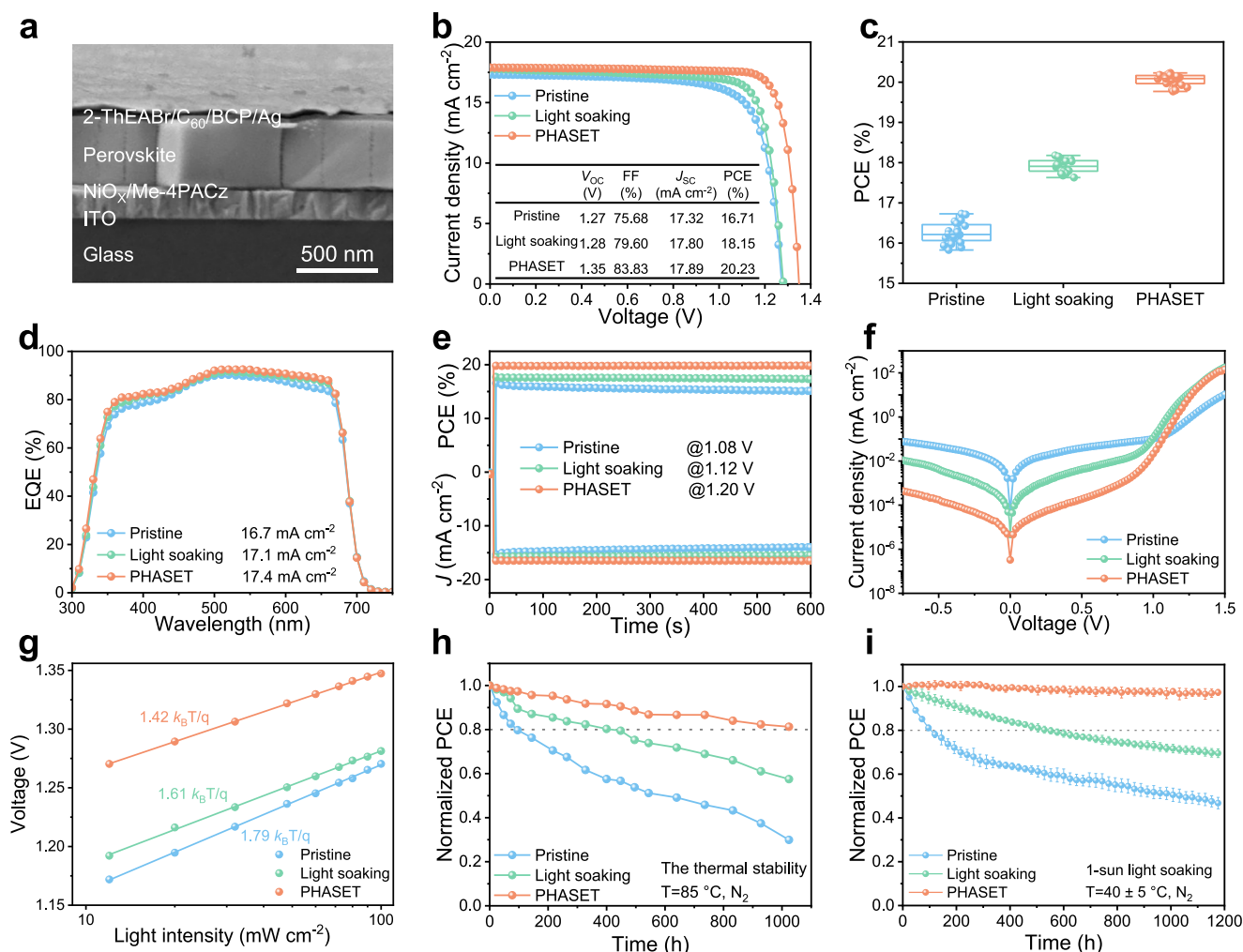


Fig. 4 | Device performance of pristine, light soaking-treated, and PHASET WBG PSCs. a Cross-sectional SEM image of a representative PHASET device. **b** J - V curves of the best-performing WBG PSCs under reverse scan. **c** Statistical distribution of the PCEs from 24 devices; error bars indicate standard deviations. **d** EQE spectra with corresponding integrated current densities. **e** Stabilized power

output and current density over 600 s, measured at the MPP voltages. **f** Dark J - V characteristics. **g** V_{OC} as a function of light intensity. **h** Thermal stability tracking of encapsulated PSCs at 85 °C. **i** Efficiency evolution of unencapsulated PSCs under continuous 1-sun white LED illumination in N_2 at -40 °C. Data represent four devices per group; error bars show standard deviations.

PHASET effectively suppresses the defect states. Taken together, PHASET treatment significantly improves perovskite thin-film quality by suppressing ion migration, reducing defect densities, enhancing crystallinity, and achieving uniform halide distribution. These advancements hold great promise for producing high-performance, stable optoelectronic devices.

To investigate the impact of the PHASET method on the photovoltaic performance of WBG PSCs, three types of device groups were prepared: pristine, light soaking-treated, and PHASET. Figure 4a shows the cross-sectional SEM images of the complete PHASET device, showing a single grain extending from the substrate to the top surface, which is similar to the reported high-efficiency WBG PSCs^{30,56}. The J - V curves under reverse scan obtained from champion PSCs under standard AM 1.5 G illumination were presented in Fig. 4b, and the corresponding photovoltaic parameters were summarized in Supplementary Table 3. The pristine device yields a PCE of 16.71%, with a V_{OC} of 1.27 V, a short circuit current density (J_{SC}) of 17.32 mA cm^{-2} , and an FF of 75.68%. The PHASET device shows a substantially increased V_{OC} of 1.35 V, a slightly improved J_{SC} of 17.89 mA cm^{-2} , and an enhanced FF of 83.83%, leading to a champion PCE of 20.23%. To our knowledge, this represents one of the highest-performing 1.79 eV perovskite solar cells. Additionally, under forward-scan J - V curves

(Supplementary Fig. 26) confirmed negligible hysteresis in the PHASET device. The 2D-treated devices, by comparison, showed an inferior PCE of 19.42%, particularly in V_{OC} (Supplementary Fig. 27). Over 20 cells were collected to confirm the parameter reproducibility for statistical comparison. As shown in Fig. 4c, the average PCE of the PHASET devices (20.06%) was significantly improved and with a narrower PCE distribution compared to that of the pristine device (16.24%) and the light soaking-treated device (17.92%). The detailed photovoltaic parameters were summarized in Supplementary Fig. 28 and Supplementary Table 4. To verify the reliability of J_{SC} , the external quantum efficiency (EQE) spectra showed that the integrated current density of pristine, light soaking-treated, and PHASET devices was 16.7, 17.1, and 17.4 mA cm^{-2} , respectively (Fig. 4d). The PHASET device showed higher quantum efficiency in the 300–400 nm and 550–650 nm ranges. The increase at shorter wavelengths can be attributed to the suppression of nonradiative recombination near the light-facing side, possibly benefited by light soaking, while improvement at longer wavelengths is due to reduced defective sites in the perovskite bulk and the 2D perovskite passivation at its top surface. Figure 4e illustrates the stabilized power output at the maximum power point (MPP) voltage, where the PHASET device maintained its PCE without degradation over 600 s, benefiting from the enhanced phase stability. In contrast, the pristine device

demonstrated slight decay over the same period. The PHASET device also displayed higher voltage and higher current at its MPP.

The dark current density of the PHASET device was nearly two orders of magnitude lower than that of the pristine device (Fig. 4f), indicating reduced leakage current due to lower defect density. To gain further insights into the suppression of nonradiative recombination, the V_{OC} dependence on light intensity was measured, as depicted in Fig. 4g. The ideality factor n can be linearly fitted by the formula $V_{OC} = \frac{nk_B T}{q} (\ln L + 1)$, where n represents the ideal factor, k_B is the Boltzmann's constant, T is the temperature, q is the elementary charge, and L represents the light intensity^{57,58}. The PHASET device had an ideality factor of 1.42, compared to 1.79 for the pristine device and 1.61 for the light soaking-treated device, indicating reduced trap-assisted recombination.

The PHASET method inhibited phase segregation in mixed-halide WBG PSCs, as demonstrated by stability tests. Under thermal conditions (85 °C, Fig. 4h), encapsulated PHASET devices retained over 80% of their initial PCE after 1000 h in a nitrogen atmosphere, whereas the light soaking-treated and pristine devices dropped below 57% and 30%, respectively. Under operational conditions (1-sun LED illumination at ~40 °C in N₂ atmosphere, Fig. 4i and Supplementary Fig. 29), unencapsulated PHASET devices maintained 97% of their initial PCE after ~1200 h, whereas the 2D-treated, light soaking-treated, and pristine devices dropped below 81%, 70%, and 47%, respectively. Post-aging analysis revealed stable PHASET device morphology (Supplementary Figs. 30 and 31), while the pristine perovskite device showed the formation of more voids and PbI₂ flakes, indicating inferior stability. The enhanced stability further confirms the advantage of the PHASET treatment to enhance the quality of the film and drive the perovskite film directly to the stabilization stage. It should be noted that the PHASET process is an early attempt to address phase segregation, and further research is needed to optimize factors such as light wavelength, exposure duration, and process improvements.

To exploit the effectiveness of these WBG perovskites, we integrated them into monolithic all-perovskite TSCs (see details in Experimental Section). The 1.25 eV FA_{0.5}MA_{0.5}Sn_{0.5}Pb_{0.5}I₃ narrow-bandgap (NBG) perovskite subcell exhibits a PCE of 20.85%, with a V_{OC} of 0.83 V, a J_{SC} of 32.58 mA cm⁻², and an FF of 77.29% (Supplementary Fig. 32a). Furthermore, the EQE spectrum of the NBG PSC (Supplementary Fig. 32b) shows an integrated J_{SC} of 31.45 mA cm⁻², which aligns well with the J_{SC} obtained from the J - V measurement. The monolithic tandem device architecture is glass/ITO/NiO_x/Me-4PACz/WBG perovskite/C₆₀/BCP/indium oxide (In₂O₃)/ITO/PEDOT:PSS/NBG perovskite/C₆₀/BCP/Ag, as shown in Fig. 5a, where the In₂O₃/ITO/PEDOT:PSS works as a robust interconnection layer (ICL). We optimized the thickness of the WBG and NBG perovskite layers to achieve current matching between the two subcells. The cross-sectional SEM image showed the optimized perovskite thicknesses are ~350 nm for WBG perovskite and ~1100 nm for NBG perovskite, respectively (Fig. 5b), and also demonstrates high crystallinity of the tandem stack.

Figure 5c shows the J - V curves under reverse scan obtained from champion TSCs with different treatments. Significant improvements in both V_{OC} and FF are observed for tandems, driven by the better performance of the WBG subcell and its improved current matching with the NBG subcell. As a result, an efficiency of 28.64% was achieved for our best-performing all-perovskite PHASET TSC, with a high V_{OC} of 2.11 V, a J_{SC} of 16.38 mA cm⁻², and an FF of 83.04% under the reverse scan; the detailed parameters are listed in Supplementary Table 5. Additionally, forward-scan J - V curves (Supplementary Fig. 33) confirmed negligible hysteresis in the PHASET TSCs. The 2D-treated devices, by comparison, showed an inferior PCE of 27.57% (Supplementary Fig. 34). The EQE-integrated J_{SC} s for WBG and NBG subcells measured from a tandem device are 16.2 and

16.1 mA cm⁻², respectively (Fig. 5d), demonstrating a well-matched current and aligning closely with the J_{SC} values obtained from the J - V measurement. Figures 5e, f and Supplementary Fig. 35 show the statistical distribution of the photovoltaic parameters based on these three treatments in the same batch. The PHASET-treated tandem devices show higher repeatability with an averaged PCE and V_{OC} of 28.23 ± 0.41% and 2.098 ± 0.007 V, respectively (Supplementary Table 6). The improvement in V_{OC} achieved by PHASET is significant and reproducible, primarily due to the enhanced V_{OC} of the WBG subcell. The tandem devices experience an additional V_{OC} loss of ~0.07 V, attributed to the ICL and tandem fabrication processes.

The PHASET-treated TSC demonstrated good device stability, maintaining a steady-state efficiency of 27.91% after 600 s of MPP tracking (Fig. 5g). Furthermore, we also performed MPP tracking of unencapsulated tandems in nitrogen (Fig. 5h and Supplementary Fig. 36). The PHASET TSC maintained 77% of its initial efficiency after about ~1200 h of continuous operation under 1-sun illumination at the MPP voltage, while the pristine, light soaking-treated, and 2D-treated tandem devices had much shorter lifetimes. This clearly suggests that the better performance and operational stability of all-perovskite TSC is mainly beneficial from the improved homogeneity and suppressed phase segregation in WBG PSC with PHASET treatment.

In summary, we investigated the mechanisms of phase segregation in WBG perovskite materials and introduced a PHASET method to enhance both device efficiency and stability. We employed high-resolution in-situ KPFM to spatially resolve topography and surface potential, revealing the dynamics of photon-induced phase segregation and its subsequent recovery process. Our comprehensive analysis, incorporating EDS and PL results, identified iodine ions as key contributors to phase segregation, with a tendency to redistribute homogeneously under light exposure. Building on this mechanistic insight, we developed a light-assisted approach to cultivate high-quality WBG perovskite films, achieving an efficiency of 20.23%. To our knowledge, it represents one of the highest-performing 1.79 eV perovskite solar cells. Importantly, the unencapsulated 1.79 eV WBG-PSC maintained 97% of its initial PCE after 1200 h of continuous light soaking in nitrogen. Moreover, we demonstrated a two-terminal all-perovskite TSC with a champion efficiency of 28.64% by integrating it with a 1.25 eV NBG perovskite subcell. The unencapsulated TSC retained 77% of its original PCE after about 1200 h of MPP tracking. These findings not only offer a deeper understanding of phase separation but also signify the PHASET method as a promising approach for advancing high-quality WBG perovskite thin-films for photovoltaic and optoelectronic applications.

Methods

Materials and solvents

N,N-dimethylformamide (DMF, 99.8%, anhydrous), dimethyl sulfoxide (DMSO, 99.9%, anhydrous), ethyl acetate (EA, 99.8%, anhydrous), isopropanol (IPA, 99.5%, anhydrous), chlorobenzene (CB, 99.9%, anhydrous), Tin (II) iodide (SnI₂, 99.99%), tin (II) fluoride (SnF₂, 99%), dopamine hydrochloride (DAHCl, 98%) and lead thiocyanate (Pb(SCN)₂, 99.5%) were obtained from Sigma-Aldrich. NiO_x nanoparticle powder (particle size around 10 nm) and Glass/ITO (8 Ω sq⁻¹) were purchased from Advanced Election Technology Company in China. Lead (II) iodide (PbI₂, 99.99%), Lead (II) bromide (PbBr₂, 99.99%), [4-(3,6-Dimethyl-9H-carbazol-9-yl)butyl]phosphonic Acid (Me-4PACz), and Guanidine thiocyanate (GuaSCN, 99%) were acquired from TCI Shanghai Chemical Industry Materials Corp. The Formamidinium iodide (FAI, 99.99%) and methylammonium iodide (MAI, 99.9%) were purchased from Greatcell Solar Materials Pty Ltd. PEDOT:PSS (CLEVIOSS P VP AI 4083) was purchased from Heraeus. Lead (II) chloride (PbCl₂, 99%), Cesium iodide (CsI, 99%), C₆₀, and 2-ThEABr were bought from Xi'an Polymer Light Technology Corp. BCP was

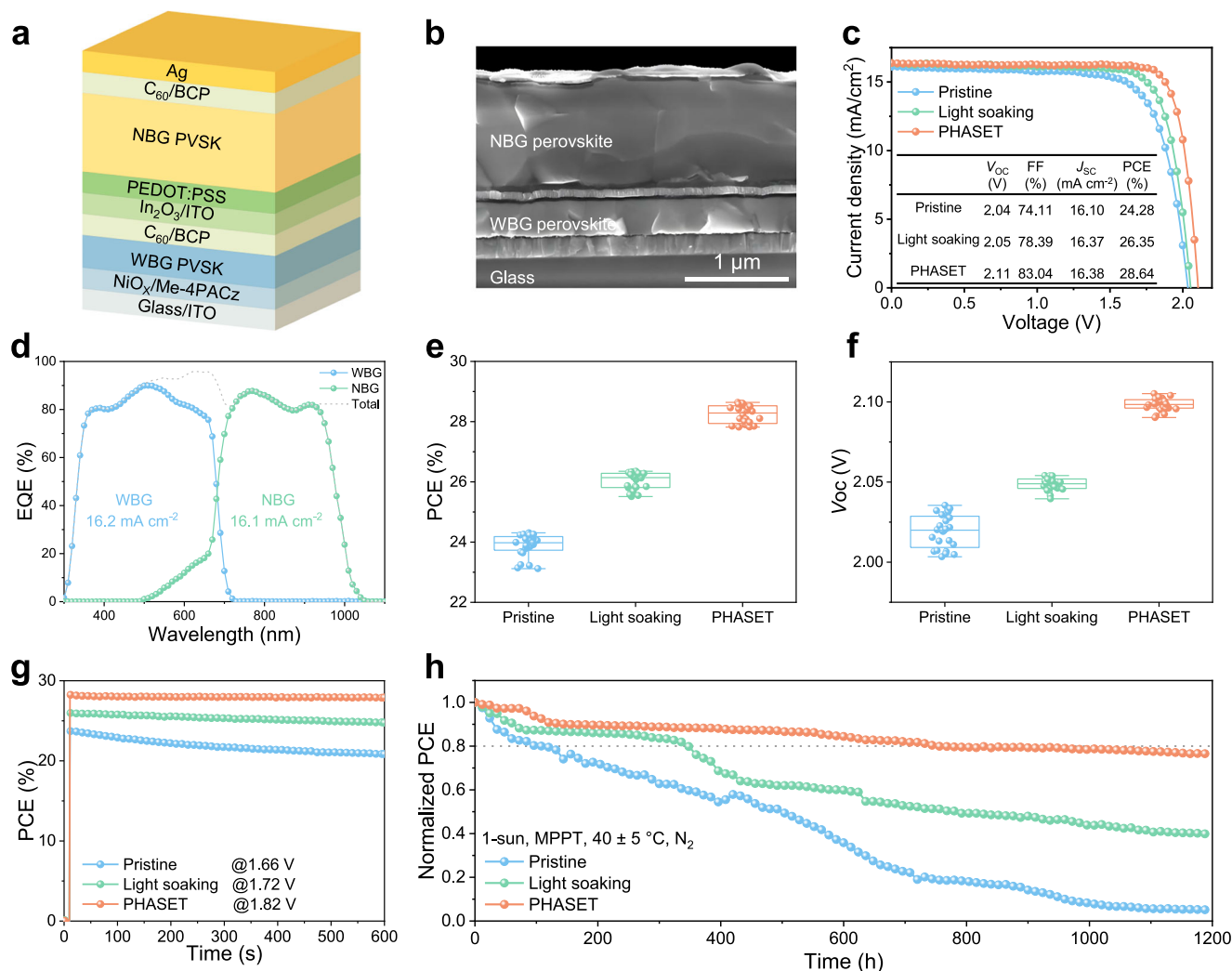


Fig. 5 | Photovoltaic performance and characterization of complete all-perovskite TSCs. a Schematic of the two-terminal all-perovskite TSC architecture. **b** Cross-sectional SEM image of a representative TSC. **c** *J*-*V* curves of the best-performing TSCs measured under reverse scan; the inset summarizes key photovoltaic parameters. **d** EQE spectra with integrated *J*_{SC} values. Statistical distributions

of **e** PCE and **f** *V*_{OC} from 24 devices; error bars represent standard deviations. **g** Stabilized power output over 600 s, measured at the MPP voltages. **h** Continuous MPP tracking of unencapsulated TSCs under continuous 1-sun white LED illumination in N₂ at -40 °C.

procured from Luminescence Technology Corp. The Indium oxide (In₂O₃) particles were purchased from Beijing Lichengxin Material Technology Corp. The Indium tin oxide (ITO, In₂O₃/SnO₂ 90/10 wt.%) target was purchased from Hebei Jiuyue Material Technology Corp. All materials used in this study were commercially available and without any purification.

Device fabrication

Precursor solution preparation

WBG Perovskite FA_{0.8}CS_{0.2}Pb(I_{0.6}Br_{0.4})₃. The WBG perovskite (1.79 eV) precursor solution (1.2 M) was prepared by dissolving 0.96 mmol FAI, 0.24 mmol CsI, 0.48 mmol PbI₂ and 0.72 mmol PbBr₂ in 1 mL mixed solvent of DMF and DMSO with a volume ratio of 4:1. Then 4.85 mg (1.5 mol% relative to Pb) Pb(SCN)₂ and 8.34 mg (3 mol% relative to Pb) PbCl₂ were added into the solution. Moreover, to study the phase segregation issue, we added 5 and 10 mol% excess PbI₂ into the solution. The perovskite precursor solution was thoroughly mixed at 55 °C for 2 h before use.

NBG Perovskite FA_{0.5}MA_{0.5}Sn_{0.5}Pb_{0.5}I₃. The NBG perovskite (1.25 eV) precursor solution (1.8 M) was prepared by dissolving

154.80 mg FAI, 143.10 mg MAI, 335.27 mg SnI₂, 414.90 mg PbI₂, 14.10 mg SnF₂, 4.25 mg GuaSCN in 1 mL DMF and DMSO with a volume ratio of 4:1. Then 0.5 mg DAHCl was dissolved in a mixed solution of CB and DMSO with a volume ratio of 4:1 to obtain a dopamine cation (DAH⁺) post-treatment precursor.

Perovskite solar cell fabrication

WBG PSCs. The perovskite solar cells were fabricated in a planar device architecture: glass/ITO/NiO_x/Me-4PACz/perovskite/C60/BCP/Ag. The ITO substrates were sonicated in deionized (DI) water, acetone, isopropanol, and ethanol for 15 min in sequence. Then, the substrates were dried with nitrogen blow and exposed to UV-ozone (UVO) treatment for 15 min to remove organic residuals on the substrates. Then the 20 mg mL⁻¹ NiO_x solution (dissolved in deionized water) was spin-coated on cleaned ITO at 4000 rpm for 20 s, followed by annealing at 100 °C for 5 min in air. Next, the substrates, which had cooled to room temperature, were transferred into a nitrogen-filled glove box. The solution of Me-4PACz (1.00 mg mL⁻¹ in IPA) was spin-coated on NiO_x film at 5000 rpm for 25 s and annealed at 100 °C for 5 min. The perovskite precursor solution was spin-coated at 5000 rpm for 40 s with 0.2 mL of EA dripped slowly at the last 15 s. And we

annealed the as-deposited films at 110 °C for 20 min. Then the film was exposed to light for a period of time (see Supplementary Note 1 for detailed steps). The 2-ThEABr solution (5 mg mL⁻¹ in IPA and stirred at 55 °C for 4 h before use) was spin-coated on the cooled perovskite top surface at 5000 rpm for 30 s, and then annealed at 100 °C for 3 min. Finally, the films were transferred to a vacuum chamber for thermal evaporation, and 30 nm C₆₀, 5 nm BCP, and 100 nm Ag were subsequently evaporated at various rates of 0.2 Å ds⁻¹, 0.2 Å s⁻¹, and 1.0 Å ds⁻¹, respectively, at a pressure of 4 × 10⁻⁴ Pa to complete the entire cell fabrication. The metal electrode was completed through a metal shadow mask with an overlapped area of 0.045 cm².

NBG PSCs. PEDOT:PSS diluted with IPA (volume ratio 1:1) was spin-coated on the ITO substrate at 4000 rpm for 30 s, followed by annealing at 150 °C for 10 min. 33 μL of perovskite precursor solution was spin-coated onto the PEDOT:PSS layer with a two-step spin-coating procedure: (i) 1000 rpm for 10 s and (ii) 4000 rpm for 40 s. 200 μL of EA was dropped onto the substrates during the second step. The prepared perovskite films were first annealed at 60 °C for 2 min, and then transferred to a 100 °C hotplate for 10 min. Then the DAH⁺ solution was spin-coated onto the cooled perovskite film at 4000 rpm for 30 s, followed by annealing at 75 °C for 10 min. For single-junction NBG PSCs, all the samples were transferred to the evaporation chamber, and the same processes were done as for WBG PSCs.

TSCs. For the fabrication of TSCs, a 20 nm In₂O₃ film was deposited on the C₆₀/BCP via electron beam evaporation at a rate of 0.05 Å ds⁻¹ in a high vacuum. Throughout the deposition process, the beam current was maintained in the range of 10 to 20 mA. Then, about 80 nm of ITO was deposited on the In₂O₃ film by radio frequency sputtering. We use a 4-inch target at room temperature with a power of 120 W under Ar pressure of 0.45 Pa. PEDOT:PSS diluted with IPA (volume ratio 1:1) was spin-coated onto the sputtered ITO layer and followed by annealing for 5 min on a 100 °C hotplate. Then, the film was transferred to a glovebox for the fabrication of an NBG subcell as described above.

Thin film and device characterization

Film characterization. The surface morphologies of various perovskite films and the cross-sectional structure of devices were attained by ZEISS Sigma 300 scanning electron microscopy (SEM) at an accelerating voltage of 5 kV. The X-ray diffraction (XRD) patterns of perovskite films were obtained using a Bruker D8 Discover A25 with Cu-Kα radiation. The UV-Vis and photoluminescence (PL) spectra were acquired using a homemade system with a fiber optic spectrometer (Ocean Optics, QE65000) and an excitation wavelength of a 532 nm laser source. The time-resolved photoluminescence (TRPL) spectra were acquired by an Edinburgh Instrument FLS920.

The KPFM and C-AFM measurements were performed on a Bruker Dimension Icon atomic force microscope (AFM) system. The AFM system and samples were kept inside an argon-filled glovebox with water and oxygen levels lower than 0.01 ppm. The KPFM system has a home-built setup including a low-noise lock-in amplifier (Signal Recovery 7208) and a negative feedback analog circuit. This configuration generated the Kelvin probe signal and consistently nullified the electrostatic force between the probe and the sample. Operating in tapping mode, the KPFM utilized a PPP-EFM tip coated with Pt-Ir, while perovskite samples were grounded to the AFM stage using silver paste.

The C-AFM measurements were performed on the same AFM system and operated in contact mode by using the PPP-EFM tip. A small bias of 1.25 V was applied to the sample, and C-AFM measures the current through the sample to the tip.

In the in-situ KPFM measurements, the topography exhibited minimal change, enabling precise probing of the same location based on topography images. For light soaking, we employed an LED cold light source with a light intensity of ~0.2 sun, minimizing temperature

increases. Light illumination occurred through the side of the AFM scanner, while for dark storage, we covered the sample surface with aluminum foil.

In the data processing, the topography images were subjected to a first-order flattening process, and the potential and current images were subjected to a zero-order flattening. All potential and current profiles were raw data without any flattening.

Performance measurements. The PSC performance was tested in a N₂ glovebox at 25 °C, under AM 1.5 G, 100 mW cm⁻² illumination generated by a solar simulator (Sol3A 94063 A, Newport). The light intensity was calibrated by a KG-5 filtered standard silicon cell (SRC-2020, NREL calibrated). The *J*-*V* curves were obtained using a source meter (Keithley 2400) with a scan rate of 0.1 V s⁻¹ for both reverse and forward directions and a scanning range of -0.1–1.4 V. The device area was defined by metal masks and set to 0.045 cm². The external quantum efficiency (EQE) spectra were measured from 300 to 1100 nm using a QE testing system (QE-R 3011, Enli Tech) without any light and voltage biasing under near-dark test conditions. For TSCs, the bias illumination from a 150 W halogen lamp with optical filters of 900 nm and 550 nm was employed to measure the spectral response of the WBG and NBG subcells, respectively. No bias voltage was applied during the EQE measurements of the TSCs. The long-term stability of the best-performed PSCs was studied on a solar cell stability test system (PURI 2400-E8, PURI Materials) under 100 mW cm⁻² illumination. The light source was a white LED lamp without a filter, and the samples were unencapsulated and tested in a N₂ environment.

Reporting summary

Further information on research design is available in the Nature Portfolio Reporting Summary linked to this article.

Data availability

The authors declare that the main data supporting the findings of this study are available within the article and its Supplementary Information files. Extra data are available from the corresponding author upon request. Source data are provided with this paper.

References

- Noh, J. H. et al. Chemical management for colorful, efficient, and stable inorganic-organic hybrid nanostructured solar cells. *Nano Lett.* **13**, 1764–1769 (2013).
- He, R. et al. Wide-bandgap organic-inorganic hybrid and all-inorganic perovskite solar cells and their application in all-perovskite tandem solar cells. *Energy Environ. Sci.* **14**, 5723–5759 (2021).
- NREL. Best research-cell efficiency chart. <https://www.nrel.gov/pv/cell-efficiency.html> (2024).
- Peng, W. et al. Reducing nonradiative recombination in perovskite solar cells with a porous insulator contact. *Science* **379**, 683–690 (2023).
- Tian, X. et al. Periodic module rejuvenation provides early market entry for circular all-perovskite tandem photovoltaic technologies. *Energy Environ. Sci.* **16**, 5551–5567 (2023).
- Hoke, E. T. et al. Reversible photo-induced trap formation in mixed-halide hybrid perovskites for photovoltaics. *Chem. Sci.* **6**, 613–617 (2015).
- Sadhanala, A. et al. Blue-Green color tunable solution processable organolead chloride-bromide mixed halide perovskites for optoelectronic applications. *Nano Lett.* **15**, 6095–6101 (2015).
- Yoon, S. J. et al. Tracking iodide and bromide ion segregation in mixed halide lead perovskites during photoirradiation. *ACS Energy Lett.* **1**, 290–296 (2016).
- Wen, J. et al. Steric engineering enables efficient and photostable wide-bandgap perovskites for all-perovskite tandem solar cells. *Adv. Mater.* **34**, 2110356 (2022).

10. Bischak, C. G. et al. Heterogeneous charge carrier dynamics in organic-inorganic hybrid materials: nanoscale lateral and depth-dependent variation of recombination rates in methylammonium lead halide perovskite thin films. *Nano Lett.* **15**, 4799–4807 (2015).
11. Huang, T. et al. Performance-limiting formation dynamics in mixed-halide perovskites. *Sci. Adv.* **7**, eabj1799 (2021).
12. Brennan, M. C. et al. Light-induced anion phase segregation in mixed halide perovskites. *ACS Energy Lett.* **3**, 204–213 (2018).
13. Yang, B. et al. Perovskite solar cells with near 100% internal quantum efficiency based on large single crystalline grains and vertical bulk heterojunctions. *J. Am. Chem. Soc.* **137**, 9210–9213 (2015).
14. Stranks, S. D. et al. Electron-hole diffusion lengths exceeding 1 micrometer in an organometal trihalide perovskite absorber. *Science* **342**, 341–344 (2013).
15. Eames, C. et al. Ionic transport in hybrid lead iodide perovskite solar cells. *Nat. Commun.* **6**, 7497 (2015).
16. Azpiroz, J. M. et al. Defect migration in methylammonium lead iodide and its role in perovskite solar cell operation. *Energy Environ. Sci.* **8**, 2118–2127 (2015).
17. Tennyson, E. M. et al. Heterogeneity at multiple length scales in halide perovskite semiconductors. *Nat. Rev. Mater.* **4**, 573–587 (2019).
18. Gratia, P. et al. Intrinsic halide segregation at nanometer scale determines the high efficiency of mixed cation/mixed halide perovskite solar cells. *J. Am. Chem. Soc.* **138**, 15821–15824 (2016).
19. Barrier, J. et al. Compositional heterogeneity in $\text{Cs}_x\text{FA}_{1-x}\text{Pb}(\text{Br}_{x-1-x})_3$ perovskite films and its impact on phase behavior. *Energy Environ. Sci.* **14**, 6394–6405 (2021).
20. Bischak, C. G. et al. Origin of reversible photoinduced phase separation in hybrid perovskites. *Nano Lett.* **17**, 1028–1033 (2017).
21. Zhao, Y. et al. Strain-activated light-induced halide segregation in mixed-halide perovskite solids. *Nat. Commun.* **11**, 6328 (2020).
22. Rehman, W. et al. Photovoltaic mixed-cation lead mixed-halide perovskites: links between crystallinity, photo-stability and electronic properties. *Energy Environ. Sci.* **10**, 361–369 (2017).
23. Muscarella, L. A. et al. Lattice compression increases the activation barrier for phase segregation in mixed-halide perovskites. *ACS Energy Lett.* **5**, 3152–3158 (2020).
24. Beal, R. E. et al. Structural origins of light-induced phase segregation in organic-inorganic halide perovskite photovoltaic materials. *Mater* **2**, 207–219 (2020).
25. Zhao, Y. et al. Suppressing ion migration in metal halide perovskite via interstitial doping with a trace amount of multivalent cations. *Nat. Mater.* **21**, 1396–1402 (2022).
26. Wang, Z. et al. Suppressed phase segregation for triple-junction perovskite solar cells. *Nature* **618**, 74–79 (2023).
27. Fu, X. et al. Halogen-halogen bonds enable improved long-term operational stability of mixed-halide perovskite photovoltaics. *Chem* **7**, 3131–3143 (2021).
28. Abdi-Jalebi, M. et al. Maximizing and stabilizing luminescence from halide perovskites with potassium passivation. *Nature* **555**, 497–501 (2018).
29. Kim, D. et al. Efficient, stable silicon tandem cells enabled by anion-engineered wide-bandgap perovskites. *Science* **368**, 155–160 (2020).
30. He, R. et al. Improving interface quality for 1-cm² all-perovskite tandem solar cells. *Nature* **618**, 80–86 (2023).
31. Wen, J. et al. Heterojunction formed via 3D-to-2D perovskite conversion for photostable wide-bandgap perovskite solar cells. *Nat. Commun.* **14**, 7118 (2023).
32. Yuan, Y. et al. Electric-Field-Driven reversible conversion between methylammonium lead triiodide perovskites and lead iodide at elevated temperatures. *Adv. Energy Mater.* **6**, 1501803 (2015).
33. Jung, H. R. et al. Surface potential mapping and n-type conductivity in organic-inorganic lead iodide crystals. *CrystEngComm* **20**, 6551–6556 (2018).
34. Kerner, R. A. et al. The role of halide oxidation in perovskite halide phase separation. *Joule* **5**, 2273–2295 (2021).
35. deQuilettes, D. W. et al. Photo-induced halide redistribution in organic-inorganic perovskite films. *Nat. Commun.* **7**, 11683 (2016).
36. Huang, K. et al. Manipulating the migration of iodine ions via reverse-biasing for boosting photovoltaic performance of perovskite solar cells. *Adv. Sci.* **9**, 04163 (2022).
37. Jiang, C.-S. et al. How grain boundaries in $\text{Cu}(\text{In,Ga})\text{Se}_2$ thin films are charged: revisit. *Appl. Phys. Lett.* **101**, 033903 (2012).
38. Nie, J. et al. Recent progress in regulating surface potential for high-efficiency perovskite solar cells. *ACS Energy Lett.* **9**, 1674–1681 (2024).
39. Ren, X. et al. Mobile iodides capture for highly photolysis- and reverse-bias-stable perovskite solar cells. *Nat. Mater.* **23**, 810–817 (2024).
40. Wan, Z. et al. Suppressing ion migration through dual interface engineering toward efficient and stable perovskite solar modules. *ACS Energy Lett.* **10**, 1585–1595 (2025).
41. Guo, Y. et al. Focusing on mixed-halide Br-rich perovskite solar cells: an inevitable open-circuit voltage deficit derived from photoinduced halide segregation?. *Mater* **5**, 2015–2030 (2022).
42. Kobayashi, E. et al. Increasing the efficiency of silicon heterojunction solar cells and modules by light soaking. *Sol. Energy Mater. Sol. Cells* **173**, 43–49 (2017).
43. Cattin, J. et al. Influence of light soaking on silicon heterojunction solar cells with various architectures. *IEEE J. Photovolt.* **11**, 575–583 (2021).
44. Schmidt, J. Light-induced degradation in crystalline silicon solar cells. *Solid State Phenom.* **95–96**, 187–196 (2003).
45. Winter, M. et al. Light and elevated temperature induced degradation and recovery of gallium-doped Czochralski-silicon solar cells. *Sci. Rep.* **12**, 8089 (2022).
46. Liu, W. et al. Light-induced activation of boron doping in hydrogenated amorphous silicon for over 25% efficiency silicon solar cells. *Nat. Energy* **7**, 427–437 (2022).
47. Chen, D. et al. Progress in the understanding of light- and elevated temperature-induced degradation in silicon solar cells: a review. *Prog. Photovolt. Res. Appl.* **29**, 1180–1201 (2020).
48. Yeo, Z. Y. et al. Status review and future perspectives on mitigating light-induced degradation on silicon-based solar cells. *Renew. Sust. Energy Rev.* **159**, 112223 (2022).
49. Du, L. et al. Indium oxide buffer layer for perovskite/Si 4-terminal tandem solar cells with efficiency exceeding 30. *J. Energy Chem.* **102**, 189–196 (2024).
50. Li, C. et al. Enhanced efficiency and stability of wide-bandgap perovskites via Br-rich bulk and surface 2D passivation for indoor photovoltaics. *Sol. Rrl.* **8**, 2400231 (2024).
51. Khenkin, M. et al. Light cycling as a key to understanding the outdoor behaviour of perovskite solar cells. *Energy Environ. Sci.* **17**, 602–610 (2024).
52. He, R. et al. Pure 2D perovskite formation by interfacial engineering yields a high open-circuit voltage beyond 1.28 V for 1.77-eV wide-bandgap perovskite solar cells. *Adv. Sci.* **9**, 2203210 (2022).
53. Li, Z. et al. Hyperbranched polymer functionalized flexible perovskite solar cells with mechanical robustness and reduced lead leakage. *Nat. Commun.* **14**, 6451 (2023).
54. Man, M. T. et al. Clarifying photoluminescence decay dynamics of self-assembled quantum dots. *Sci. Rep.* **9**, 4613 (2019).
55. Chirvony, V. S. et al. Interpretation of the photoluminescence decay kinetics in metal halide perovskite nanocrystals and thin polycrystalline films. *J. Lumin.* **221**, 117092 (2020).

56. Lin, R. All-perovskite tandem solar cells with 3D/3D bilayer perovskite heterojunction. *Nature* **620**, 994–1000 (2023).
57. Zhu, J. et al. A donor-acceptor-type hole-selective contact reducing non-radiative recombination losses in both subcells towards efficient all-perovskite tandems. *Nat. Energy* **8**, 714–724 (2023).
58. Meng, R. et al. Reductive 2D capping layers through dopamine salt incorporation for Pb-Sn mixed perovskite solar cells. *ACS Energy Lett.* **8**, 5206–5214 (2023).

Acknowledgements

This work is supported by National Natural Science Foundation of China (52102304, 52302327, and 52172238), Open Project of Shaanxi Laboratory of Aerospace Power (2021SXSYS-01-03), and the Fundamental Research Funds for the Central Universities (3102019JC0005). This project is also partially supported by the International Cooperation Project of CAS (181GJHZ202412MI, 181GJHZ2024092FN), the International Cooperation Project of Ningbo City (2024H034).

Author contributions

C.X. and Z.L. conceived the idea and directed this project. L.D. and F.C. planned experiments and coordinated the work. L.D. fabricated WBG devices and tandems for performance and fabricated perovskite films for characterization. R.M. fabricated NBG devices and tandems. L.D. and F.C. wrote the original draft. L.D. carried out optical spectroscopy of films and devices and performed data analysis. F.C. and Y.Z. carried out KPFM and data analysis. J.Z., Z.G., C.C., C.L., D.Z., and J.Y. assisted with device analysis and data interpretation. C.L., Z.L., and C.X. secured funding and edited the manuscript. All authors discussed the results and commented on the paper.

Competing interests

The authors declare no competing interests.

Additional information

Supplementary information The online version contains supplementary material available at <https://doi.org/10.1038/s41467-025-63176-w>.

Correspondence and requests for materials should be addressed to Zhen Li or Chuanxiao Xiao.

Peer review information *Nature Communications* thanks the anonymous, reviewer(s) for their contribution to the peer review of this work. A peer review file is available.

Reprints and permissions information is available at <http://www.nature.com/reprints>

Publisher's note Springer Nature remains neutral with regard to jurisdictional claims in published maps and institutional affiliations.

Open Access This article is licensed under a Creative Commons Attribution-NonCommercial-NoDerivatives 4.0 International License, which permits any non-commercial use, sharing, distribution and reproduction in any medium or format, as long as you give appropriate credit to the original author(s) and the source, provide a link to the Creative Commons licence, and indicate if you modified the licensed material. You do not have permission under this licence to share adapted material derived from this article or parts of it. The images or other third party material in this article are included in the article's Creative Commons licence, unless indicated otherwise in a credit line to the material. If material is not included in the article's Creative Commons licence and your intended use is not permitted by statutory regulation or exceeds the permitted use, you will need to obtain permission directly from the copyright holder. To view a copy of this licence, visit <http://creativecommons.org/licenses/by-nc-nd/4.0/>.

© The Author(s) 2025